Theoretical and experimental determination of *K*- and *L*-shell x-ray relaxation parameters in Ni

M. Guerra,[1,*] J. M. Sampaio,[2] F. Parente,[1] P. Indelicato,[3] P. Hönicke,[4] M. Müller,[4] B. Beckhoff,[4] J. P. Marques,[5] and J. P. Santos[1]

[1]*Laboratório de Instrumentação, Engenharia Biomédica e Física da Radiação (LIBPhys-UNL), Departamento de Física, Faculdade de Ciências e Tecnologia, FCT, Universidade Nova de Lisboa, 2829-516 Caparica, Portugal*

[2]*LIP – Laboratório de Instrumentação e Física Experimental de Partículas, Av. Prof. Gama Pinto 2, 1649-003 Lisboa, Portugal*

[3]*Laboratoire Kastler Brossel, Sorbonne Université, CNRS, ENS-PSL Research University, Collége de France, Case 74; 4, place Jussieu, F-75005 Paris, France*

[4]*Physikalisch-Technische Bundesanstalt (PTB), Abbestraße 2-12, 10587 Berlin, Germany*

[5]*BioISI – Biosystems & Integrative Sciences Institute, Faculdade de Ciências da Universidade de Lisboa, Campo Grande, C8, 1749-016 Lisboa, Portugal*

(Received 23 December 2017; published 9 April 2018)

Fluorescence yields (FY) for the Ni *K* and *L* shells were determined by a theoretical and an experimental group within the framework of the International Initiative on X-ray Fundamental Parameters (FPs) collaboration. Coster-Kronig (CK) parameters were also measured for the *L* shell of Ni. Theoretical calculations of the same parameters were performed using the Dirac-Fock method, including relativistic and QED corrections. The experimental values for the FY and CK were determined at the PTB laboratory in the synchrotron radiation facility BESSY II, Berlin, Germany, and are compared to the corresponding calculated values.

DOI: 10.1103/PhysRevA.97.042501

I. INTRODUCTION

Nickel is a transition metal with very low reactivity with oxygen, which explains why about 6% of its production is used for corrosion-resistant plating. Nevertheless, its main industrial usage (around 60%) is on the production of stainless steel. Ni is one of the four elements that have ferromagnetic properties at room temperature, and its combination with aluminum and cobalt gives rise to high coercivity permanent magnets. Before the invention of rare-earth magnets, the AlNiCo alloys were among the most powerful magnets ever constructed. Due to its high magnetic permeability, it is suitable for shielding of sensitive electronic apparatus against low frequency magnetic noise. In conjunction with Fe, Cu, Cr, and Mo it forms an alloy, labeled mu-metal, which has the advantage over other high permeability materials of being very ductile, allowing it to be formed into thin metal sheets.

Ni is also of high astrophysical interest due to the fact that it is one of the final products of Si burning in massive stars prior to the supernova explosions. The striking evidence of the presence of Ni is that the light curves of type Ia supernovas are powered by the radioactive decay of ^{56}Ni to ^{56}Co at early times. The presence of Ni *K* emission lines has also been observed in active galatic nucleus (AGN), with unprecedented resolution by the XMM-Newton space observatory. A systematic study of these data to obtain the Ni-to-Fe $K\alpha$ line intensity ratios was performed recently by Fukazawa *et al.* [1] for the particular case of Seyfert galaxies. These authors discuss the possibility of a Ni-to-Fe abundance enhancement relative to the solar abundance in the surrounding torus of AGN, with implications in the models of galaxy dynamics and star formation.

Due to its almost ubiquitous presence in electronics and mechanical gears in scientific apparatus, it sometimes appears as an impurity in spectra obtained with most x-ray spectrometers. Hence, the knowledge of x-ray fundamental parameters (FPs) of Ni is highly important in the evaluation of the systematics of x-ray based techniques, such as particle induced x-ray spectroscopy (PIXE), x-ray fluorescence (XRF) spectroscopy, electron probe microanalysis (EPMA), etc.

Over the last decades, there has been an effort in remeasuring and recalculating atomic fundamental parameters such as fluorescence yields, line energies, and widths, as well as line ratios, due to the large discrepancies found in the literature. In fact, the uncertainties in the available x-ray FPs are now the main source of uncertainty in x-ray spectrometry data analysis [2]. This has led to the creation of an European project, labeled *International Initiative on X-ray Fundamental Parameters* [3], to reanalyze all of the x-ray relaxation parameters. This work is part of this initiative and consists of a comparative study of some x-ray fundamental parameters of Ni that were obtained by a joint effort between the Lisbon theoretical group and the PTB experimental group.

Besides the highly used results of Krause [4] of 1979, there are several tabulated values for the Ni *K*-shell FY, such as those of Roos [5] and Hubbell [6], compiled in the 1960s and 1970s. Several other values were obtained since 2000, among these are the experimental measurements of Şimşek *et al.* in 2000 [7], Durak *et al.* in 2001 [8], Yashoda *et al.* in 2005 [9], Öz *et al.* in 2006 [10], Han *et al.* in 2009 [11], Söğüt in 2010 [12], and

*mguerra@fct.unl.pt

Kaçal *et al.* in 2015 [13]. Other highly cited results are those of the xraylib database [14], based on data from Krause [4] (for L shell the data is identical to Krause's), McGuire [15], and Chen *et al.* [16], and those of McGuire from 1971 [15] from which we can also obtain FY results for the individual L subshells. Subshell resolved experimental values are much harder to find in the literature. In fact, we were only able to find one other paper on the Coster-Kronig yields of the L shell of Ni [17], and none on the L-shell FY (apart from the recommended values of Krause [4].

A. Ground state electronic configuration

In the literature there is still a debate over whether the Ni ground state configuration is $[\mathrm{Ar}]3d^8 4s^2$ or $[\mathrm{Ar}]3d^9 4s$ [18]. This is due to the fact that the fine structure of these configurations gives rise to two sets of states with energies that are highly overlapping. It is now generally accepted that the lowest energy level of Ni is the $[\mathrm{Ar}]3d^8 4s^2\ {}^3F_4$, however, the $[\mathrm{Ar}]3d^9 4s\ {}^3D_4$ level stands only 0.0254 eV above the ground energy [19], which means that in experiments at room temperature that level will certainly be highly populated. The highest energy level corresponding to the $[\mathrm{Ar}]3d^9 4s$ configuration is ${}^1D_2$ and is located only 0.4228 eV above the ground level. Curiously, the average energy of the levels in the configuration $[\mathrm{Ar}]3d^9 4s$ is actually lower than that of the $[\mathrm{Ar}]3d^8 4s^2$ configuration, which is the reason why the former is sometimes quoted as being the ground state configuration of Ni [18]. This property of Ni becomes very important when considering x-ray spectral fitting and/or quantification of samples at room temperature, either gaseous or solid. In fact, as the average thermal energy $\frac{3}{2}k_B T$ at 25 °C is around 0.0388 eV, both states will be highly populated, and any scattering experiment will have to take this into account.

Typical experiments for the measurement of FPs in the x-ray regime use either a radiation source or a particle beam in order to create holes in the inner shells of the element under study, and the distribution of these holes across the states space will be highly influenced by the element's initial state [20]. Therefore, if one wishes to compare theoretical and experimental FP values, or even wants to perform some data analysis from the x-ray spectra, the set of calculated FPs to use has to be chosen carefully.

B. Chemical shifts and alloying

There is a major difference in the methodology and even in the physical processes of a theoretical calculation, usually based on atomic structure calculations of isolated atoms, and an experimental determination of the FPs which usually relies on x-ray irradiation of bulk materials. Moreover, it has been frequently seen that in $3d$ transition metals the valence-electron configurations in alloys is even more disparate when compared with pure metals, and it has been shown that these differences arise from the delocalization and/or charge transfer mechanisms [11,21]. Namely, the observed change of the valence-electron configuration in Ni alloys can be explained by the transference of $3d$ electrons from Ni to the other element(s) and the rearrangement of electrons between the $3d$ and $4s$ or $4p$ orbitals of the individual metal. This rearrangement can also be seen by investigating the bond lengths of $3d$ metal complexes [22,23], which are consistent with a covalent bond being made by the $4s$ electrons, with little or no contribution from $3d$ electrons. This means that the ground electronic level of molecular Ni should resemble more the atomic first excited level than its ground level [24], as described in Sec. I A. From $K\beta/K\alpha$ x-ray intensity ratios one can estimate the change in electronic configuration when going from the isolated atom to pure metals and alloys. Since the changes of the $3d$ electron population of the transition metal, due to chemical and/or solid state effects, will modify $3p$ orbitals more than $2p$ orbitals, it will result in a change of the $K\beta/K\alpha$ x-ray intensity ratio of the metal. In fact, Han *et al.* [11] have shown through this method that, in pure Ni metal, the evaluated occupation number of the $3d$ orbitals is 9.5218 while that of $4s$ or $4p$ orbitals is 0.4782, once again confirming a deviation from the ground state of isolated Ni atoms. Other FPs, such as fluorescence and CK yields, are also shown to be dependent on the chemical environment as, for example, in alloying, as shown by Aylikci *et al.* in several works on transition metals [21,25,26]. In fact, in Krause's paper [4], he states that "*...little is known about the exact dependence of the yields, or transitions rates, on the chemical structure for these light elements* [$Z \leqslant 30$]. *It is with this caveat that the values for condensed matter listed in table 1 should be used.*", hence, in Tables II and III we have presented not only the recommended values for isolated atoms but also for condensed matter.

II. THEORY

All theoretical calculations of this work were performed with the relativistic general purpose multiconfiguration Dirac-Fock code (MCDFGME) developed by Desclaux and Indelicato [27,28].

A. Relativistic calculations

K- and L-shell x-ray fundamental parameters, such as line energies and widths, as well as FY and CK yields, were calculated using the code in the single-configuration approach because the approximation used for the evaluation of the radiationless decay rates cannot be used in an optimized levels (OL) calculation with correlation orbitals. First-order retardation terms of the Breit interaction and the Uelhing contribution to the vacuum polarization terms were included in the self-consistent field calculation, and the Wichmann-Kroll and Kallen-Sabry contributions, higher-order Breit retardation terms, as well as other QED effects, such as self-energy, were included as perturbations [29–31]. A more detailed description of the Hamiltonian and the self-consistent field procedure can be obtained in [29,32–34]. In order to calculate the wave functions and respective energies of the levels involved in all possible radiative and radiationless transitions, we have used the OL method, considering full relaxation of both initial and final states, hence providing more accurate energies and wave functions. Since the spin orbitals of the initial and final levels were optimized separately, they are not orthogonal. In order to deal with the nonorthogonality of the wave functions, the code uses the formalism described by Löwdin [35] in the calculation of radiative decay rates.

In what concerns the radiationless decay rates, we have assumed a two-step process, in which the decay process is

independent from the ionization. In this way, the electron that is ejected in the ionization process does not interact with the Auger electron, and the core hole state interacts very weakly with the later electron, which allows for the transition rates to be calculated from perturbation theory.

For radiationless decay rates to be calculated, the initial state wave functions were generated for configurations that contain one initial inner-shell vacancy while final state wave functions were generated for configurations that contain two higher shell vacancies. Continuum-state wave functions were obtained by solving the Dirac-Fock equations with the same atomic potential of the initial state, normalized to represent one ejected electron per unit energy. As explained above, in order to keep consistency between the radiative and radiationless calculations, multiconfiguration wave functions beyond intermediate coupling were not employed. Because the calculations of these atomic FPs usually require hundreds of thousand of transitions between levels with one- and two-hole configurations, a software suite was programmed to deal with the level energies, transition rates, and partial sums for the FP calculations. In this suite, all one- and two-hole configurations are built by default from the ground state configuration obtained with the DF method by Rodrigues *et al.* [36]. Nevertheless, due to the arguments stated in Secs. IA and IB, an extra calculation of all fundamental parameters was performed assuming the alternative ground state configuration [Ar] $3d^9 4s$.

B. Decay rates, subshell widths, and fluorescence and CK yields

To calculate fluorescence, Auger, and CK yields we compute the width of an atomic level i given by $\Gamma_i = \hbar \sum_j W_{ij}$, where W_{ij} is the transition probability from level i to level j, including contributions from radiative and radiationless processes. The width is then given by the sum of the radiative $\Gamma_{\rm R}$, Auger $\Gamma_{\rm A}$, and Coster-Kronig $\Gamma_{\rm CK}$ widths.

If the system has a closed outer shell, or if the interaction between the inner hole and the valence electrons is neglected, each one-hole configuration corresponds to only one level. Therefore, the width of the configuration is just the width of the corresponding level.

The situation is more complicated, in general, if the interaction of the core hole with existing unpaired electrons is taken into account. The fine structure resulting from the interaction between the inner hole and those electrons leads to a number of different levels for a given configuration, each one identified by a particular value of the total angular momentum J and by the electronic coupling [37,38]. In the case of the ground configuration of Ni, [Ar] $3d^8 4s^2$, the interaction of the inner hole with the $3d$ electrons gives rise to a large set of levels, while for the configuration [Ar] $3d^9 4s$ the number of possible couplings is somewhat lower (about half) than for the previous case, due to it having only one hole in the $3d$ shell.

Assuming that the initial levels in the one hole subshell S_n, with total angular momentum J_i, are statistically populated, the radiative (R) width of the subshell S_n is obtained by summing the partial widths $\Gamma^{\rm R}_{i,j}$ for all levels i of the system with one hole in this subshell decaying radiatively to all levels j of the system with one hole in a higher subshell

$$\Gamma^{\rm R}_{S_n} = \frac{\sum_{i,j} (2J_i + 1)\Gamma^{\rm R}_{i,j}}{\sum_i (2J_i + 1)}, \tag{1}$$

where the usual definition applies,

$$\Gamma^{\rm R}_{i,j} = \hbar W^{\rm R}_{i,j}. \tag{2}$$

Here $W^{\rm R}_{i,j}$ is the radiative transition probability from level i to level k. As in the radiative case, the radiationless width of the subshell S_n is given by

$$\Gamma^{\rm NR}_{S_n} = \frac{\sum_{i,k} (2J_i + 1)\Gamma^{\rm NR}_{i,k}}{\sum_i (2J_i + 1)}, \tag{3}$$

where

$$\Gamma^{\rm NR}_{i,k} = \hbar W^{\rm NR}_{i,k}. \tag{4}$$

Here $W^{\rm NR}_{i,k}$ is the radiationless transition probability from level i to level k. Thus, $\Gamma^{\rm NR}_{i,k}$ is the partial width corresponding to the radiationless transition from the level i in the one-hole system in subshell S_n to the level k of the system with two holes in the same or higher shells or subshells, with the emission of an electron to the continuum.

From here on, S_n will denote a one hole subshell (K, $L_{1,2,3}$, or $M_{1,,5}$), and the index i will span all possible initial levels. The final one- and two-hole system levels, corresponding to radiative and radiationless transitions, respectively, will be henceforth denoted by the indexes j or k.

Radiationless widths include contributions from Auger, Coster-Kronig, and super-Coster-Kronig transitions. Although all of these processes are sometimes labeled jointly as Auger transitions, in our work we have followed the definitions presented in Refs. [37,39]. In the Auger contributions, the initial configuration hole is filled by an electron from a higher shell, and a second electron also from a higher shell is emitted to the continuum; in the Coster-Kronig contributions, the initial hole is filled by an electron from the same shell and the emitted electron belongs to a higher shell or to another subshell of the same shell. The later are called super-Coster-Kronig transitions. Thus, the (total) width of a S_n subshell is given by

$$\Gamma_{S_n} = \Gamma^{\rm R}_{S_n} + \Gamma^{\rm NR}_{S_n}. \tag{5}$$

The FY of the atomic subshell S_n is defined as the probability that the vacancy in that subshell is filled through a radiative transition, and, if we neglect other modes of decay with very low probabilities, such as two photon transitions, hyperfine induced transitions, etc., it is given by

$$\omega_{S_n} = \frac{\Gamma^{\rm R}_{S_n}}{\Gamma^{\rm R}_{S_n} + \Gamma^{\rm NR}_{S_n}}. \tag{6}$$

Similarly to the fluorescence yield, the Auger yield a_{S_n} for the S_n subshell is defined as

$$a_{S_n} = \frac{\Gamma^{\rm NR_A}_{S_n}}{\Gamma^{\rm R}_{S_n} + \Gamma^{\rm NR}_{S_n}}, \tag{7}$$

where the width $\Gamma^{\rm NR_A}_{S_n}$ refers only to Auger transitions. On the other hand, the Coster-Kronig $f_{S_{n,n'}}$ yield for S subshell (either L, M, or N) is given by a similar expression

$$f_{S_{n,n'}} = \frac{\Gamma^{\rm NR_{CK}}_{S_n}}{\Gamma^{\rm R}_{S_n} + \Gamma^{\rm NR}_{S_n}}, \tag{8}$$

but, in this equation, only CK transitions are included in the width $\Gamma^{\rm NR_{CK}}_{S_n}$.

From these definitions, one can conclude that the following relation is valid for each subshell S_n:

$$\omega_{S_n} + a_{S_n} + \sum_{n'>n} f_{S_{n,n'}} = 1. \quad (9)$$

The theoretical linewidth for a transition between a one-hole configuration S_n and another one-hole configuration S'_m is given by

$$\Gamma_{S_n \to S'_m} = \Gamma_{S_n} + \Gamma_{S'_m}. \quad (10)$$

Although, as explained before, when unpaired outer electrons exist, instead of having only one level corresponding to a one-hole configuration, the interaction between the inner hole and the outer unpaired electrons gives rise to a usually large set of levels. Hence, the usual label *level* width [40] should be changed to *subshell* width, and when the set of levels within a given configuration spans widely over an energy region, the simple sum of the level widths in the initial and final configurations, to obtain a linewidth, is a poor estimation of the real width value [37]. This is the case of Ni, where eight $3d$ electrons exist in the ground state, and nine $3d$ and one $4s$ electrons exist in the other studied configuration.

III. EXPERIMENT

All experiments for the FP determinations in this work were performed at beamlines [41,42] within the PTB laboratory at the BESSY II synchrotron radiation facility in Berlin [43]. The x-ray spectrometry group of PTB operates several XRF endstations [44,45], which are equipped with radiometrically calibrated instrumentation and thus allow for a reference-free quantitative XRF analysis [46]. By employing both transmission and XRF experiments on free-standing thin-foil samples, the reference-free XRF setups of PTB also allow for an experimental determination of FPs [47–49].

A. Nickel *L*-shell fluorescence yields and Coster-Kronig factors

The measured sample in this work is a thin free-standing foil of 500 nm nickel which was irradiated with monochromatic synchrotron radiation at several incident photon energies. Calibrated photodiodes were used to measure the incident as well as the transmitted radiation to determine the radiant power of the incident beam and the transmittance of the sample in a broad photon energy range from 550 to 1800 eV. The x-ray emission of the sample was measured by a grating spectrometer which is able to measure the emitted photons in an energy range from 730 to 1070 eV simultaneously. The energy of the incident beam was varied between 845 and 1300 eV for the emission measurements, with increased point density in the vicinity of the nickel L-absorption edges. The grating spectrometer was calibrated with respect to the product of detection sensitivity ϵ, and solid angle of detection Ω, as well as to its response behavior. In order to derive the fluorescence intensity from the measured spectra, the x-ray emission of the sample was modeled, convoluted with the response functions and fitted by a least-square optimization. Figure 1 shows a fitted spectrum of Ni excited above the L_1-absorption edge. Using experimentally determined response functions allows for the discrimination of real spectral features and detector artifacts. Details about the spectrometer and the fitting of the measured spectra can be found in [50].

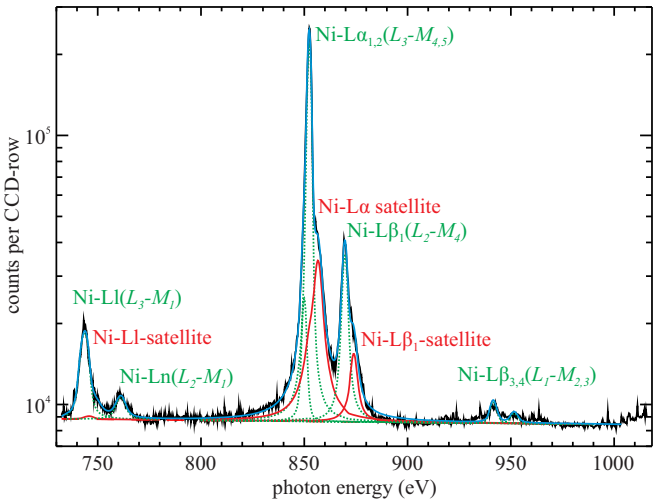

FIG. 1. X-ray emission spectrum of the 500 nm free-standing nickel foil. The energy of the exciting radiation was 1030 eV which is above the L_1-absorption edge. The fitted model spectrum is plotted in green, the fluorescence lines in blue and satellite lines in red.

Using the Sherman equation for a thin sample [44] we can calculate the measured count rate $CR_{S_n,S_{n'}}$ of an x-ray line corresponding to an electron decaying to subshell S_n from subshell $S_{n'}$ with the corresponding photon energy $E_{S_n,S_{n'}}$ as follows:

$$CR_{S_n,S_{n'}} = N(E_k)\varepsilon(E_{S_n,S_{n'}})\frac{\Omega}{4\pi} \times \frac{\gamma_{\text{in}}\rho\sigma_{S_n,S_{n'}}(E_k)d}{\gamma_{\text{in}}\rho\mu(E_k)d + \gamma_{\text{out}}\rho\mu(E_{S_n,S_{n'}})d} \times (1 - e^{\gamma_{\text{in}}\rho\mu(E_k)d}e^{\gamma_{\text{out}}\rho\mu(E_{S_n,S_{n'}})d}), \quad (11)$$

The incident photon flux $N(E_k)$ was derived from the measured radiant power at the incident photon energy E_k of the plane grating monochromator [41]. The two geometry factors γ_{in} and γ_{out} are $1/\sin(45°)$ because of the 45/45-deg beam geometry. Other symbols are τ_{S_n} for the photoelectric mass absorption coefficient of subshell S_n, μ for the mass absorption coefficient, $T_{L\alpha}$ for the probability of the $L\alpha$ (L_3-$M_{4,5}$) transition, and d for the thickness of the sample. The calculation of the fluorescence production factor depends on the energy of the exciting radiation and its position relative to the absorption edges. In the case of the $L\alpha$ fluorescence multiplet we get the following equations:

$$\begin{aligned}
\sigma_{L\alpha}(E_k) &= T_{L\alpha}\omega_{L_3}\tau_{L_3}(E_k), \quad E_{L_3} < E_k < E_{L_2}, \\
\sigma_{L\alpha}(E_k) &= T_{L\alpha}\omega_{L_3}[\tau_{L_3}(E_k) + f_{L_{23}}\tau_{L_2}(E_k)], \; E_{L_2} < E_k < E_{L_1}, \\
\sigma_{L\alpha}(E_k) &= T_{L\alpha}\omega_{L_3}[\tau_{L_3}(E_k) + f_{L_{23}}\tau_{L_2}(E_k) + f_{L_{12}}f_{L_{23}}\tau_{L_1}(E_k) \\
&\quad + f_{L_{13}}\tau_{L_1}(E_k)], \; E_{L_1} < E_k. \quad (12)
\end{aligned}$$

The goal was to obtain the subshell fluorescence yields ω_{S_n} and the Coster-Kronig factors $f_{S_n,S_{n'}}$ without using tabulated values for τ_{S_n} and μ because of the high uncertainties of these fundamental parameters. In particular, the uncertainties of the photoelectric cross sections are not well known and

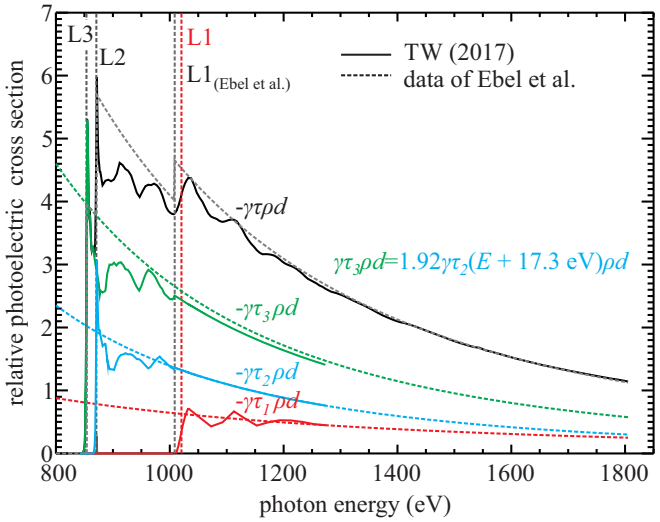

FIG. 2. The partial photoelectric cross sections (PECS) derived from the transmission measurements of the thin Ni foil. Only relative cross sections were determined, the thickness d of the sample is not needed to calculate the fluorescence yields and Coster-Kronig factors.

are mostly estimated in the soft x-ray range. Furthermore, the absorption fine structure is not included in the majority of databases. Hence, we introduced an additional factor d in Eq. (11), which allows us to obtain the factors $\gamma\rho\mu d$ directly from our transmittance measurements under 45° geometry:

$$e^{\gamma_{\rm in}\rho\mu(E_{\rm in})d} = \frac{I_{\rm trans}}{I_{\rm in}}. \tag{13}$$

It is also sufficient to derive the photoelectric cross section (PECS) in a relative way only. In particular, it is sufficient to derive the factors $\gamma\rho\tau_{S_n}d$ which we will call relative PECS. First, the total of the relative PECS $\gamma\rho\tau d$ was derived from the factor $\gamma\rho\mu d$ by subtracting the extrapolated contribution of the other shells (M, N) and the scattering cross sections (<0.3%). The extrapolation was done by an exponential function which was fitted to the measured $\gamma\rho\mu d$ between 550 and 800 eV below the L_3 absorption edge. The resulting total of the relative PECS is plotted in black in Fig. 2. Next we separated the relative PECS of the subshells L_3 and L_2 ($\gamma\rho\tau_{L_3}d$ and $\gamma\rho\tau_{L_2}d$) by assuming that the absorption fine structure of the two subshells, which are both p orbital, is similar. Hence, we used the first part of the relative L_3 PECS below the L_2 edge to model the first part of the relative L_2 PECS just above the L_2 edge. In Fig. 2 the relative L_3 PECS are plotted in blue and the relative L_2 PECS in red. The ratio between the L_2 and the L_3 PECS and the energy offset between the two edges was fitted by a least-squares procedure. The resulting ratio of 1 : 1.92 is in good agreement with the expected value of 1 : 2 for the population ratio between the $2p_{1/2}$ and the $2p_{3/2}$ orbitals. Above the L_1 edge the partial PECS of Ebel *et al.* [51] were used to extrapolate the contributions of L_3 and L_2, see the dashed lines in Fig. 2. In the energy range between 1300 and 1850 eV the factor $\gamma\rho d$ between the data of Ebel and the measured total of the relative PECS was averaged. Using this factor with the PECS of Ebel, a good agreement with our relative PECS, which were derived below the L_1 edge, was found at the L_1 edge. In the case of the L_2 PECS the difference was less than 1% and for the L_3 it was about 4.5%. For the extrapolation above the L_1 edge the L_3 cross section of Ebel was reduced by 4.5%. With this interpolation the L_1 part of the photoelectric absorption could be derived, see the difference between the blue solid line and the blue dashed line in Fig. 2.

To calculate the Coster-Kronig factors and the partial fluorescence yields, the derived fluorescence line and satellite line intensities were summed up to total fluorescence intensities I_{L_i} for each subshell. Fluorescence measurements were performed at many energies of the exciting radiation between and above the absorption edge energies E_{L_i}. Equation (14) was used to calculate the Coster-Kronig factor $f_{L_{23}}$ for each pair of energy points between L_3 and L_2 and between L_2 and L_1, the same equation was used for the $f_{L_{12}}$ but with energies between L_2 and L_1 and above L_1 and the count rates CR_{L_2} of the L_2 subshell. Equation (15), which allows for the calculation of the factor $f_{L_{13}}$, is more complex due to the dependency of the CR_{L_3} to the other two Coster-Kronig factors. This has also a huge impact on the uncertainties of $f_{L_{13}}$. The relative uncertainty of the derived PECS of the L_3 shell ranges from 1.5% to 3.7% from below the L_3 edge to far above the edge. In case of the L_2 shell the relative uncertainty of the PECS is 5.6% at maximum. Due to the small jump at L_1 edge and the relative uncertainty of the PECS of the L_1 shell resulting from the fit is 15%. The uncertainty of the Coster-Kronig factors is mainly caused by the uncertainties of the relative PECS. The standard uncertainty of $f_{L_{23}}$ is 0.10 but the uncertainty of $f_{L_{12}}$ and $f_{L_{13}}$ is 0.23 and 0.3, respectively, more than double of $f_{L_{23}}$ because of the higher uncertainty of the L_2 and L_1 PECS and because of several subtractions and the dependency to $f_{L_{23}}$ in Eq. (15). In Table III the resulting average of the three Coster-Kronig factors are listed. Please note that in case of $f_{L_{13}}$ we cannot distinguish between the radiative and nonradiative transitions:

$$f_{L_{23}} = \frac{\gamma\rho\tau_{L3}(E_2)d}{\gamma\rho\tau_{L2}(E_2)d}\left[\frac{\gamma\rho\tau_{L3}(E_1)d}{CR_{L3}(E_1)}\frac{CR_{L3}(E_2)}{\gamma\rho\tau_{L3}(E_2)d}\right], \tag{14}$$

$$f_{L_{13}} = \frac{\gamma\rho\tau_{L3}(E_3)d}{\gamma\rho\tau_{L1}(E_3)d}\left[\frac{\gamma\rho\tau_{L3}(E_1)d}{CR_{L3}(E_1)}\frac{CR_{L3}(E_3)}{\gamma\rho\tau_{L3}(E_3)d} - \left(1 + f_{L_{23}}\frac{\gamma\rho\tau_{L2}(E_3)d}{\gamma\rho\tau_{L3}(E_3)d}\right)\right] - f_{L_{12}}f_{L_{23}}, \tag{15}$$

with $E_1 < E_{L_2}$, $E_2 > E_{L_2}$, and $E_3 > E_{L_1}$. All parameters which are needed to calculate the partial fluorescence yields are now known. Solving Eq. (11) for the three partial fluorescence yields is akin to normalize the fluorescence count rates to the probability that a hole in the respective subshell was created by photoionization or by a Coster-Kronig transition. These probabilities depend on the energy of the exciting radiation and are given by the relative PECS $\gamma\rho\tau_{S_n}d$ plus the enhancement due to Coster-Kronig transitions between subshells $S_{n'}$ and S_n which is the ratio $f_{S_n,S_{n'}}\gamma\rho\tau_{S_n}d/\gamma\rho\tau_{S_{n'}}d$. In Fig. 3 the values of the partial fluorescence yields obtained for each excitation energy, which was used in the fluorescence measurements, are plotted. Apart from the near edge region, the resulting yields are nicely constant as expected. That means we have no remaining energy dependency except slightly above the absorption edges, which is a good indication that the determination of the Coster-Kronig factors and the relative PECS was successful.

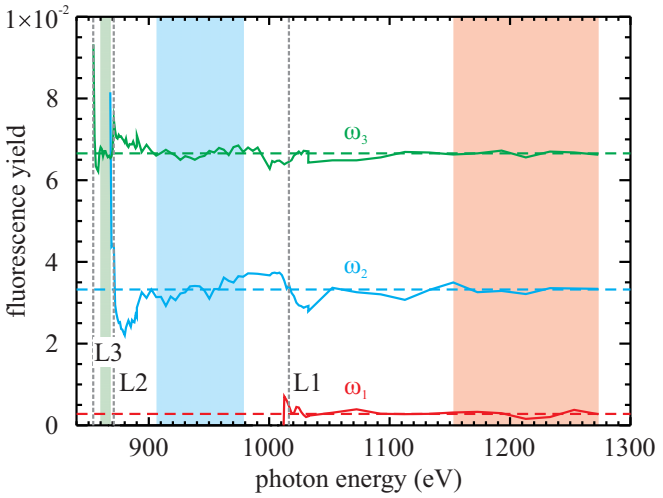

FIG. 3. Derived partial fluorescence yields for each subshell. The final values (dashed lines) are averages performed in the regions that are color marked (blue for ω_{L_3} and red for ω_{L_2} and ω_{L_1}).

To finally determine the partial fluorescence yields, the single values were averaged in the energy ranges where they are well constant, the ranges are marked in Fig. 3, blue for ω_{L_3} and red for ω_{L_2} and ω_{L_1}. The main contributions to the relative uncertainties are the calibration of the grating spectrometer (4.5%) and the determination of the relative PECS (1.5%–5.7%). The impact of the measured count rate statistics is low for L_3 and L_2, but dominating for L_1 because of the very low count rate of the $L_{\beta_{3,4}}$ line with a relative uncertainty of 25%. Details about the uncertainties can be found in [52]. The results for fluorescence yields of the three L subshells are shown in Table II.

B. Nickel K-shell fluorescence yield

The K-shell FPs of Ni were experimentally determined in a similar manner. Both the transmission and the emitted fluorescence intensities for Ni $K\alpha$ and Ni $K\beta$ radiation were measured for various monochromatic incident photon energies around the K attenuation edge of Ni. A free-standing 500 nm Ni foil was used for these experiments at the FCM beamline of PTB [42]. The applied experimental procedures follow our earlier works on the experimental determination of the O-K [53] and the Ti-K shell [49] fluorescence yields as well as the previously described determination of the L-shell fluorescence yields. From the measured transmission of the foil, experimental values for the self-attenuation of the foil as well as the PECS can be derived. In contrast to the L-shell experiments, we used a calibrated silicon drift detector (SDD) [54] for the detection of the fluorescence radiation. From a spectral deconvolution of the recorded x-ray fluorescence spectra and the calibrated efficiencies of the used SDD detector, the fluorescence intensities for Ni-$K\alpha$ and Ni-$K\beta$ radiation can be determined. Together with the other known instrumental and experimental parameters, e.g., the solid angle of detection and the incident photon flux, the fluorescence production cross sections for Ni-$K\alpha$ and Ni-$K\beta$ of the used thin foil can be quantified. Using the previously determined PECS for the Ni-K shell, the Ni-K fluorescence yield can then be derived from this data. The resulting value is shown in Table I. The main contributors to the stated uncertainty budget are the attenuation correction factor and the determination of the photoelectric cross section. Further details can be found in [55].

TABLE I. K-shell FY for Ni. Results are compared with available literature values. Experimental uncertainties are indicated within parentheses.

Study	ω_K
TW (expt.) (2017)	0.410(14)
TW (theor.) $3d^8 4s^2$ (2017)	0.425(13)
TW (theor.) $3d^9 4s$ (2017)	0.413(12)
Kaçal *et al.* (2015)	0.427(26)
xraylib (2011)	0.412
Söğüt *et al.* (2010)	0.451(45)
Han *et al.* (2009)	0.435(35)
Öz (2006)	0.421(4)
Yashoda *et al.* (2005)	0.408(15)
Durak *et al.* (2001)	0.412(15)
Şimşek (2000)	0.448(14)
Krause (1979)	0.406(20)
Hubbell *et al.* (1975)	0.418(11)
Roos (1957)	0.366(11)

IV. RESULTS AND DISCUSSION

The theoretical fluorescence and CK yields were calculated from Eq. (6) using the radiative and radiationless transition rates calculated within the Dirac-Fock framework, as explained in Sec. II. Calculations were performed for the K and L shells of Ni, and the results are presented in Tables I, II, and III, along with the most recent experimental results, as well as the recommended results of Krause [4] and those from xraylib [14] (for L shell in condensed matter they are the same, and hence are not shown). The first thing that stands out from our results is that, for the K-shell FY, there is an excellent agreement between our theoretical and experimental results with the results from other authors, with the exception of those measured by Roos in 1957 [5] and Şimşek *et al.* in 2000 [7]. Regarding the latter, the authors state in their paper that "We think that there is an experimental error in the measurement of Ni.", while in the former, the employed method relies on fixed K jump ratios which at that time were obtained with nonrelativistic computations. It is also clear that the influence of the initial configuration on the K-shell FY calculation is very small, about 0.5% only, while for the L shell the differences increase up to 4%. This was expected because in the K-shell FY calculation, there is a large contribution from $K \rightarrow L$ transitions, diluting the contribution of $K \rightarrow M,N$ transitions, which are more affected by the difference in the valence configuration. Also, the fact that Auger and radiative transitions are affected by this effect in a similar way, and the FY is a ratio of both, the valence configuration does not effectively alter the K-shell FY. This is not true for the L subshells as the weight of the transitions between L subshells

TABLE II. L-shell FY for Ni. Results are compared with available literature values. Experimental uncertainties are indicated within parentheses.

Study	ω_{L1}	ω_{L2}	ω_{L3}
TW (expt.) (2017)	$2.8(9) \times 10^{-4}$	$3.3(3) \times 10^{-3}$	$6.7(4) \times 10^{-3}$
TW (theor.) $3d^8 4s^2$ (2017)	$6.71(20) \times 10^{-4}$	$9.64(29) \times 10^{-3}$	$8.24(25) \times 10^{-3}$
TW (theor.) $3d^9 4s$ (2017)	$6.54(20) \times 10^{-4}$	$9.25(28) \times 10^{-3}$	$8.50(26) \times 10^{-3}$
Krause (isolated atom) (1979)	$1.4(4) \times 10^{-3}$	$8.6(22) \times 10^{-3}$	$9.3(24) \times 10^{-3}$
Krause (condensed matter) (1979)		$5.1(13) \times 10^{-3}$	
McGuire (1971)	4.63×10^{-4}		8.02×10^{-3}

and $M_{4,5}$ and N_1 is higher, also enhancing the effect of the valence configuration in the calculated FY.

For the CK yields, the differences in values obtained from the two initial configurations increase substantially, especially $f_{L_{23}}$, for which we found a 55% change, essentially due to the reasons stated above. For $f_{L_{12}}$ and $f_{L_{13}}$ using both configurations we found a 9% and 0.5% discrepancy, respectively. This has also to do, in part, with the fact that from the [Ar] $3d^9 4s$ initial configuration, there are no Auger transitions to a final two-hole configuration in the 4s subshell. Apart from this, we see also that there is a huge increase, when going from the [Ar] $3d^8 4s^2$ to the [Ar] $3d^9 4s$ initial configuration, in the partial radiationless yield corresponding to Auger transitions of the type L_2-$M_5 M_5$ and L_2-$M_5 N_1$ (if energetically possible). This fivefold increase is then compensated by the observed fivefold $f_{L_{23}}$ decrease, resulting in an almost unchanged L_2 Auger yield. Regarding the comparison of our experimental results with both our and other group's theoretical values, we observe large discrepancies. Our experimental ω_{L_1} value is less than half of our theoretical results and five times lower than that recommended by Krause (for isolated atoms). Comparing to the value of McGuire, it is around 35% lower. Concerning our ω_{L_2} measurement, we observe a 2.9 times decrease when compared to our theoretical results and to the recommended value of Krause for the isolated atom, which is comparable with our theoretical results. Comparing our experimental ω_{L_2} FY to the condensed matter value of Krause we see a 35% difference, which is almost comparable to its intrinsic uncertainty. For ω_{L_3} our experimental result is around 23% to 27% lower than both our theoretical results but around 40% lower than those of Krause (isolated atom). Our theoretical values, however, compare very well to the free atom calculations of McGuire and the recommended values of Krause also for an isolated atom. The discrepancies are higher if one considers the CK yields, for which we see a 2.6–2.9-fold higher experimental result for the $f_{L_{12}}$ than both our theoretical results, an $f_{L_{13}}$ experimental value which is one order of magnitude smaller than our theoretical results, and an $f_{L_{23}}$ value that is more than two orders of magnitude higher than our theoretical value for the [Ar] $3d^8 4s^2$ valence configuration. Still, when comparing our $f_{L_{12}}$ theoretical results with those of Krause, Sorensen, and McGuire, we see a very good agreement, maybe slightly favoring the valence [Ar] $3d^8 4s^2$ configuration. For $f_{L_{13}}$ CKY we find once again that they are comparable with the free atom results of the other authors. Although Krause's $f_{L_{23}}$ recommended value, in condensed matter, is more than two orders of magnitude higher than our theoretical estimates, its uncertainty interval overlaps with our experimental interval. Regarding the source of the discrepancies for the CK yields, it is well known that the chemical bonds in the metallic sample will induce quite substantial changes in the shapes and energies of the wave functions of the outer shells. For example, for an isolated Ni atom, regarding the $f_{L_{23}}$ CK yields, only the L_2-$L_3 N_1$ transitions are energetically allowed, amounting to a total of 470 transitions. Due to the extra-atomic relaxation effects induced by neighboring atoms in the metal, the level energies might shift quite a large amount, thus enabling Auger channels that are forbidden for an isolated atom. We have not performed a similar calculation to that of Yin *et al.* [56], because in order to do so, one has to artificially assign values for the kinetic energy of the ejected electron which are completely arbitrary. For example, Yin *et al.* have assumed for all of the L_2-$L_3 M_{4,5}$ Auger transitions, a kinetic energy of 10 eV for Cu and 5 eV for Zn without any explanation why. If our level energies were off by as much as 10 eV, we would see a rise in the number of allowed Auger transitions from 470 to 1043 which, connected to the fact that the Coster-Kronig transition probabilities rise very rapidly as a function of the ejected electrons kinetic energy [56], would result in a rise of the $f_{L_{23}}$ CK yield by several orders of magnitude. Since $f_{L_{12}}$, $f_{L_{13}}$, and $f_{L_{23}}$ are interconnected by the relation given by Eq. (9), we would see a corresponding change in $f_{L_{12}}$ and $f_{L_{13}}$.

TABLE III. CK yields for the L shell of Ni. Experimental uncertainties are indicated within parentheses.

Study	$f_{L_{12}}$	$f_{L_{13}}$	$f_{L_{23}}$
TW (expt.) (2017)	0.82(23)	0.06(30)	0.66(10)
TW (theor.) $3d^8 4s^2$ (2017)	0.317(9)	0.644(19)	0.00331(9)
TW (theor.) $3d^9 4s$ (2017)	0.288(9)	0.641(19)	0.00150(5)
Krause (isolated atom) (1979)	0.30(5)	0.55(6)	0.028(11)
Krause (condensed matter) (1979)			0.45(18)
Sorensen (1991)	0.35(20)	0.5(2)	0.6(2)
McGuire (1971)	0.325	0.622	

Regarding the uncertainties related to the theoretical methods, we have estimated the uncertainty of the FY to be less than 3%, by error propagation of Eq. (6). The individual uncertainty of the partial width $\Gamma^{\mathrm{R}}_{S_n}$ was obtained as the average of the differences in transition rates between the length and the velocity gauge, weighted by the transition rates themselves. Due to the impossibility of using the same procedure for Auger rates, but bearing in mind that the quality of the wave functions should be similar for two-hole states, we have adopted for the uncertainty of $\Gamma^{\mathrm{NR}}_{S_n}$ the same value as the uncertainty of

radiative partial width. This leads to final uncertainties of around 1% for ω_K and less than 3% in the FYs for the L_1, L_2, and L_3 subshells for the initial configuration [Ar] $3d^8 4s^2$ and slightly lower for the [Ar] $3d^9 4s$ initial configuration, hence we adopt the value of 3% for the uncertainty of all shells as presented in all tables. The uncertainties related to the experimental methods are briefly described in Sec. III. They are calculated by error propagation of the basic uncertainties of all measurements and of the data analysis procedures such as the fitting of the high-resolution spectra. A detailed description of the uncertainty assessment can be found in [55] and [50,52] for the FY of the K-shell and the L-shell parameters, respectively. The achieved relative uncertainty of the K FY is 3.4% only. In the case of the L shell the FY of L_3 has the lowest relative uncertainty with 6% because of its direct accessibility by the measurements which have been performed at incident photon energies between the L_3 and the L_2 absorption edges. The L_2 and L_1 parameters have significantly higher uncertainties because of the more complex data analysis and in the case of the CK yields also because of the strong dependencies on the other CK yields.

V. CONCLUSIONS

In this work we have presented the results of a collaboration between an experimental and a theoretical group, within the International Initiative on X-ray Fundamental Parameters framework, to obtain fluorescence and Coster-Kronig yields for the K and L shells of Ni. The Dirac-Fock method, including relativistic and QED corrections, has been used to obtain the wave functions and binding energy values, as well as, K- and L-shell fluorescence and Coster-Kronig yields. The influence on the valence configuration of Ni in the calculated FP, which might suffer modifications due to chemical and solid state effects, was also investigated and we found that substantial changes might occur, especially concerning CK yields. Although our theoretical and experimental K-shell results are in agreement, large discrepancies between theory and experiment were found for the L-shell fluorescence and CK yields, which may be due to factors like the condensed matter effects within the bulk metal samples, not taken in account in the calculations. In fact, the similarity of the experimental results, both ours and those from Sorensen *et al.*, with Krause's recommended values for condensed matter, strongly suggests that L_2-$L_3M_{4,5}$ Auger transitions will be energetically possible in the solid metal as opposed to the isolated atom where only L_2-L_3N_1 are allowed. The good results for the FY of the K shell encourage us to calculate more elements to reanalyze a broad range from transition metals to medium Z elements. Furthermore, we want to test the calculations for lower Z elements such as oxygen or carbon. To validate such calculations, the available instrumentation, which is radiometrically calibrated, can be used to measure the relevant parameters reliably with well-known uncertainties. In the case of the L-shell parameters, the use of the calibrated high-resolution spectrometer allows for reliable measurements of FY and CK yields. Most of the parameters could be measured with a sufficiently low uncertainty, only the CK yields of the L_1 subshell are too high for a good comparison. Only correct calculations supported by reliable and accurate measurements can make the goal of the International Initiative on X-ray Fundamental Parameters to reanalyze all x-ray relaxation parameters feasible. In the case of the K shell the presented theoretical and experimental techniques fulfill these requirements. To access the L-shell parameters, the presented techniques have to be improved further. While it is clear that the theoretical results are based on the assumption of free atoms, whereas the experimental work is related to atoms in solids, the effect of this difference on inner shells is much smaller than for outer shells. Hence, the good agreement for the K-shell parameters lend support to the conclusion that the methods employed, both experimental and theoretical, are quite accurate. So for outer shells, the theoretical results can be accepted with some confidence in the context of free atoms while the experimental results are valid for atoms in solids.

ACKNOWLEDGMENTS

M. Guerra acknowledges the support of the FCT, under Contract No. SFRH/BPD/92455/2013. This work was supported in part by the research center Grants No. UID/FIS/04559/2013 to LIBPhys-UNL, and No. UID/MULTI/04046/2013 to BioISI, from the FCT/MCTES/PIDDAC. Laboratoire Kastler Brossel is "Unité Mixte de Recherche du CNRS, de l' ENS et de l'UPMC" No. 8552. Parts of this work have been carried out in the framework of the Project 14IND01 3DMetChemIT, funded by the EMPIR program, co-financed by the Participating States and from the European Union's Horizon 2020 research and innovation program.

[1] F. Yasushi, F. Shunya, H. Kazuma, O. Masanori, H. Kazuyoshi, and N. Hirofumi, Fe-K line time variability and Ni abundance of distant reflectors in Seyfert galaxies, Astrophys. J. **821**, 15 (2016).

[2] R. M. Rousseau, Detection limit and estimate of uncertainty of analytical XRF results, Rigaku J. **18**, 33 (2001).

[3] FP Initiative, Roadmap document on atomic Fundamental Parameters for X-ray methodologies - version 2, (2017), http://www.exsa.hu/news/wp-content/uploads/IIFP_Roadmap_V1.pdf.

[4] M. O. Krause, Atomic radiative and radiationless yields for K and L shells, J. Phys. Chem. Ref. Data **8**, 307 (1979).

[5] C. E. Roos, K fluorescence yield of several metals, Phys. Rev. **105**, 931 (1957).

[6] J. H. Hubbell, W. J. Veigele, E. A. Briggs, R. T. Brown, D. T. Cromer, and R. J. Howerton, Atomic form factors, incoherent scattering functions, and photon scattering cross sections, J. Phys. Chem. Ref. Data **4**, 471 (1975).

[7] O. Şimşek, O. Doğan, U. Turgut, and M. Ertuğrul, Measurement of K shell fluorescence yields of some elements in the atomic range $22 \leqslant Z \leqslant 30$ using photoionisation, Radiat. Phys. Chem. **58**, 207 (2000).

[8] R. Durak and Y. Özdemir, Measurement of K-shell fluorescence cross-sections and yields of 14 elements in the atomic number

range $25 \leqslant Z \leqslant 47$ using photoionization, Radiat. Phys. Chem. **61**, 19 (2001).

[9] T. Yashoda, S. Krishnaveni, and R. Gowda, Measurement of K-shell fluorescence yields for the elements in the range $22 \leqslant Z \leqslant 52$ excited by 14.4 and 122 keV photons, Nucl. Instrum. Methods Phys. Res. Sect. B **240**, 607 (2005).

[10] E. Öz, Determination of ratios of emission probabilities of Auger electrons and KL-shell radiative vacancy transfer probabilities for 17 elements from Mn to Mo at 59.5 keV, J. Quant. Spectrosc. Radiat. Transfer **97**, 41 (2006).

[11] I. Han and L. Demir, Valence-electron configuration of Fe, Cr, and Ni in binary and ternary alloys from $K\beta$-to-$K\alpha$ x-ray intensity ratios, Phys. Rev. A **80**, 052503 (2009).

[12] O. Söğüt, Investigation of the K shell fluorescence yields of Cr, Mn, Fe, Co, Ni, Cu, Zn, Mo, Ag, Cd, Ba, La, Ce, and their compounds, Chin. J. Phys. **48**, 212 (2010).

[13] M. R. Kaçal, I. Han, and F. Akman, Determination of K shell absorption jump factors and jump ratios of 3d transition metals by measuring K shell fluorescence parameters, Appl. Rad. Isotopes **95**, 193 (2015).

[14] T. Schoonjans, A. Brunetti, B. Golosio, M. Sanchez del Rio, V. A. Solé, C. Ferrero, and L. Vincze, The xraylib library for x-ray-matter interactions. Recent developments, Spectrochim. Acta Part B **66**, 776 (2011).

[15] E. J. McGuire, Atomic L-shell Coster-Kronig, Auger, and radiative rates and flourescence yields for Na-Th, Phys. Rev. A **3**, 587 (1971).

[16] M. H. Chen, B. Crasemann, and H. Mark, Widths and fluorescence yields of atomic L-shell vacancy states, Phys. Rev. A **24**, 177 (1981).

[17] S. L. Sorensen, S. J. Schaphorst, S. B. Whitfield, B. Crasemann, and R. Carr, L -shell Coster-Kronig transition probabilities in Ni, Cu, and Mo measured with synchrotron radiation, Phys. Rev. A **44**, 350 (1991).

[18] E. R. Scerri, *The Periodic Table: Its Story and Its Significance* (Oxford University Press, New York, 2007).

[19] A. Kramida, Yu. Ralchenko, J. Reader, and NIST ASD Team, *NIST Atomic Spectra Database (version 5.5.3)* (National Institute of Standards and Technology, Gaithersburg, MD, 2018).

[20] P. Hönicke, M. Kolbe, M. Müller, M. Mantler, M. Krämer, and B. Beckhoff, Experimental Verification of the Individual Energy Dependencies of the Partial L-Shell Photoionization Cross Sections of Pd and Mo, Phys. Rev. Lett. **113**, 163001 (2014).

[21] N. K. Aylikci, J. M. Sampaio, A. Kahoul, V. Aylikci, I. H. Karahan, M. Guerra, J. P. Santos, J. P. Marques, and E. Tirașoğlu, The investigation of K-shell fluorescence parameters of ZnFe alloys with different grain size and microstrain values, X-Ray Spectrom. **46**, 242 (2017).

[22] P. Pyykko and M. Atsumi, Molecular single-bond covalent radii for elements 1-118, Chem. Eur. J. **15**, 186 (2009).

[23] M. Guerra, P. Amaro, J. P. Santos, and P. Indelicato, Relativistic calculations of screening parameters and atomic radii of neutral atoms, At. Data Nucl. Data Tables **117-118**, 439 (2017).

[24] J. C. Pinegar, J. D. Langenberg, C. A. Arrington, E. M. Spain, and M. D. Morse, Ni2 revisited: Reassignment of the ground electronic state, J. Chem. Phys. **102**, 666 (1995).

[25] N. K. Aylikci, E. Tirașoğlu, I. H. Karahan, V. Aylikci, M. Eskil, and E. Cengiz, Alloying effect on K x-ray intensity ratios, K x-ray production cross-sections and radiative Auger ratios in superalloys constitute from Al, Ni and Mo elements, Chem. Phys. **377**, 100 (2010).

[26] E. Cengiz, Z. Biyiklioğlu, N. Küp Aylikci, V. Aylikci, G. o. Apaydin, E. Tirașoğlu, and H. Kantekin, Chemical effect on K shell x-ray fluorescence parameters and radiative Auger ratios of Co, Ni, Cu, and Zn complexes, Chin. J. Chem. Phys. **23**, 138 (2010).

[27] J. P. Desclaux, A multiconfiguration relativistic DIRAC-FOCK program, Comput. Phys. Commun. **9**, 31 (1975).

[28] P. Indelicato and J. Desclaux, MCDFGME, a Multiconfiguration Dirac-Fock and General Matrix Elements program (2005), http://dirac.spectro.jussieu.fr/mcdf.

[29] P. Indelicato, O. Gorceix, and J. P. Desclaux, Multiconfigurational Dirac-Fock studies of two-electron ions. II. Radiative corrections and comparison with experiment, J. Phys. B **20**, 651 (1987).

[30] O. Gorceix, P. Indelicato, and J. P. Desclaux, Multiconfiguration Dirac-Fock studies of two-electron ions. I. Electron-electron interaction, J. Phys. B **20**, 639 (1987).

[31] P. Indelicato, Multiconfiguration Dirac-Fock calculations of transition energies in two electron ions with $10 \leqslant Z \leqslant 92$, Nucl. Instrum. Methods Phys. Res. Sect. B **31**, 14 (1988).

[32] P. Indelicato and J. P. Desclaux, Multiconfiguration Dirac-Fock calculations of transition energies with QED corrections in three-electron ions, Phys. Rev. A **42**, 5139 (1990).

[33] P. Indelicato, Projection operators in multiconfiguration Dirac-Fock calculations: Application to the ground state of heliumlike ions, Phys. Rev. A **51**, 1132 (1995).

[34] P. Indelicato, Correlation and Negative Continuum Effects for the Relativistic $M1$ Transition in Two-Electron Ions using the Multiconfiguration Dirac-Fock Method, Phys. Rev. Lett. **77**, 3323 (1996).

[35] P.-O. Löwdin, Quantum theory of many-particle systems. I. Physical interpretations by means of density matrices, natural spin-orbitals, and convergence problems in the method of configurational interaction, Phys. Rev. **97**, 1474 (1955).

[36] G. C. Rodrigues, P. Indelicato, J. P. Santos, P. Patté, and F. Parente, Systematic calculation of total atomic energies of ground state configurations, At. Data Nucl. Data Tables **86**, 117 (2004).

[37] M. Guerra, J. M. Sampaio, T. I. Madeira, F. Parente, P. Indelicato, J. P. Marques, J. P. Santos, J. Hoszowska, J. C. Dousse, L. Loperetti, F. Zeeshan, M. Muller, R. Unterumsberger, and B. Beckhoff, Theoretical and experimental determination of L-shell decay rates, line widths, and fluorescence yields in Ge, Phys. Rev. A **92**, 022507 (2015).

[38] K. Kozioł, MCDF-RCI predictions for structure and width of x-ray line of Al and Si, J. Quant. Spectrosc. Radiat. Transfer **149**, 138 (2014).

[39] J. M. Sampaio, M. Guerra, F. Parente, T. I. Madeira, P. Indelicato, J. P. Santos, and J. P. Marques, Calculations of photo-induced x-ray production cross-sections in the energy range 1–150 keV and average fluorescence yields for Zn, Cd and Hg, At. Data Nucl. Data Tables **111-112**, 67 (2016).

[40] J. L. Campbell and T. Papp, Widths of the atomic K-$N7$ levels, At. Data Nucl. Data Tables **77**, 1 (2001).

[41] F. Senf, U. Flechsig, F. Eggenstein, W. Gudat, R. Klein, H. Rabus, and G. Ulm, A plane-grating monochromator beamline for the PTB undulators at BESSY II, J. Synchrotron Radiat. **5**, 780 (1998).

[42] M. Krumrey and G. Ulm, High-accuracy detector calibration at the PTB four-crystal monochromator beamline, Nucl. Instrum. Methods Phys. Res. Sect. A **467-468**, 1175 (2001).

[43] B. Beckhoff, A. Gottwald, R. Klein, M. Krumrey, R. Müller, M. Richter, F. Scholze, R. Thornagel, and G. Ulm, A quarter-century of metrology using synchrotron radiation by PTB in Berlin, Phys. Status Solidi B **246**, 1415 (2009).

[44] M. Kolbe, B. Beckhoff, M. Krumrey, and G. Ulm, Thickness determination for Cu and Ni nanolayers: Comparison of completely reference-free fundamental parameter-based x-ray fluorescence analysis and x-ray reflectometry, Spectrochim. Acta, Part B **60**, 505 (2005).

[45] J. Lubeck, B. Beckhoff, R. Fliegauf, I. Holfelder, P. Hönicke, M. Müller, B. Pollakowski, F. Reinhardt, and J. Weser, A novel instrument for quantitative nanoanalytics involving complementary x-ray methodologies, Rev. Sci. Instrum. **84**, 045106 (2013).

[46] B. Beckhoff, Reference-free x-ray spectrometry based on metrology using synchrotron radiation, J. Anal. Atom. Spectrom. **23**, 845 (2008).

[47] B. Beckhoff and G. Ulm, Determination of fluorescence yields using monochromatized undulator radiation of high spectral purity and well-known flux, Adv. X-Ray Anal. **44**, 349 (2001).

[48] M. Kolbe, P. Hönicke, M. Müller, and B. Beckhoff, L-subshell fluorescence yields and Coster-Kronig transition probabilities with a reliable uncertainty budget for selected high- and medium-Z elements, Phys. Rev. A **86**, 042512 (2012).

[49] M. Kolbe and P. Hönicke, Fundamental parameters of Zr and Ti for a reliable quantitative x-ray fluorescence analysis, X-Ray Spectrom. **44**, 217 (2015).

[50] M. Müller, B. Beckhoff, R. Fliegauf, and B. Kanngießer, Nickel L_{III} fluorescence and satellite transition probabilities determined with an alternative methodology for soft-x-ray emission spectrometry, Phys. Rev. A **79**, 032503 (2009).

[51] H. Ebel, R. Svagera, M. F. Ebel, A. Shaltout, and J. H. Hubbell, Numerical description of photoelectric absorption coefficients for fundamental parameter programs, X-Ray Spectrom. **32**, 442 (2003).

[52] M. Müller, High-resolution soft x-ray emission spectrometry, Ph.D. thesis, Technische Universität Berlin, Fakultät II - Mathematik und Naturwissenschaften, 2010.

[53] P. Hönicke, M. Kolbe, M. Krumrey, R. Unterumsberger, and B. Beckhoff, Experimental determination of the oxygen K-shell fluorescence yield using thin SiO_2 and Al_2O_3 foils, Spectrochim. Acta Part B **124**, 94 (2016).

[54] F. Scholze and M. Procop, Modelling the response function of energy dispersive x-ray spectrometers with silicon detectors, X-Ray Spectrom. **38**, 312 (2009).

[55] Y. Ménesguen, M.-C. Lépy, P. Hönicke, M. Müller, R. Unterumsberger, B. Beckhoff, J. Hoszowska, J.-C. Dousse, W. Blachucki, Y. Ito, M. Yamashita, and S. Fukushima, Experimental determination of x-ray atomic fundamental parameters of nickel, Metrologia **55**, 56 (2018).

[56] L. I. Yin, I. Adler, M. H. Chen, and B. Crasemann, Width of atomic L_2 and L_3 vacancy states near $Z = 30$, Phys. Rev. A **7**, 897 (1973).